

Computing Lagrangian coherent structures from their variational theory

Mohammad Farazmand¹ and George Haller^{2,1}

¹Department of Mathematics and Statistics, McGill University, 817 Sherbrooke St. West, Montreal, Quebec H3A 2K6, Canada

²Department of Mechanical Engineering, McGill University, 817 Sherbrooke St. West, Montreal, Quebec H3A 2K6, Canada

(Received 21 October 2011; accepted 9 February 2012; published online 9 March 2012)

Using the recently developed variational theory of hyperbolic Lagrangian coherent structures (LCSs), we introduce a computational approach that renders attracting and repelling LCSs as smooth, parametrized curves in two-dimensional flows. The curves are obtained as trajectories of an autonomous ordinary differential equation for the tensor lines of the Cauchy-Green strain tensor. This approach eliminates false positives and negatives in LCS detection by separating true exponential stretching from shear in a frame-independent fashion. Having an explicitly parametrized form for hyperbolic LCSs also allows for their further in-depth analysis and accurate advection as material lines. We illustrate these results on a kinematic model flow and on a direct numerical simulation of two-dimensional turbulence. © 2012 American Institute of Physics.

[<http://dx.doi.org/10.1063/1.3690153>]

Lagrangian coherent structures (LCSs) are time-evolving surfaces that shape trajectory patterns in complex dynamical systems, such as geophysical flows and multi-body problems. A rigorous detection of such surfaces from unsteady velocity data has only been provided recently by a variational theory of hyperbolic LCSs. This theory locates key material structures as locally most repelling or attracting material surfaces that form the skeleton of observed tracer patterns. Here, we develop a numerical algorithm that implements variational LCS theory for two-dimensional flows, rendering attracting and repelling LCSs in a smoothly parametrized form. This numerical algorithm enables the accurate detection of hyperbolic LCSs in high-end applications, such as forecasting the spread of environmental contamination.

I. INTRODUCTION

Lagrangian coherent structures are skeletons of observed tracer patterns in dynamical systems, such as those describing the evolution of fluid particles in a two-dimensional physical domain. While such centerpieces of trajectory patterns have been well understood for steady and time-periodic flows (see, e.g., Ottino²¹), exploring similar structures in unsteady flows with general time dependence, especially over a finite time-interval, has been an ongoing effort.

A number of diagnostic tools have been proposed to interpret Lagrangian pattern formation in general unsteady flows (see, e.g., Provenzale,²⁴ Boffetta *et al.*,³ Peacock and Dabiri,²³ and Broer⁴ for reviews). Among these, finite-time Lyapunov exponents (FTLE) have enjoyed broad popularity in recent years, with ridges of the FTLE field routinely considered as indicators of hyperbolic (i.e., attracting or repelling) LCSs (Haller¹³ and Shadden *et al.*²⁶). A closer look, however, reveals that FTLE ridges can produce both false

positives and negatives in LCS detection even in simple two-dimensional steady flows, let alone in complex data sets (Haller¹⁴).

Using LCSs for reliable now-casting and forecasting requires sufficient and necessary conditions that are backed by mathematical theorems. Such conditions were recently obtained in Haller,¹⁴ where the original definition of hyperbolic LCSs as locally most repelling or attracting surfaces (see Haller and Yuan¹⁶) was explored further analytically. Solving this extremum problem, Haller¹⁴ derived a variational LCS theory that provides sufficient and necessary conditions for hyperbolic LCSs in terms of the invariants of the Cauchy-Green strain tensor. For the first time, this theory separates material surfaces generating exponential stretching from those generating shear in a frame-independent fashion, thereby offering a rigorous alternative to previously proposed diagnostic quantities.

In this paper, we develop a numerical algorithm that implements the variational LCS theory of Haller¹⁴ and Farazmand and Haller⁹ for two-dimensional flows defined over a finite time-interval. The algorithm described here captures hyperbolic LCSs as smoothly parametrized material lines, obtained as trajectories of an autonomous ordinary differential equation for the tensor lines of the Cauchy-Green strain tensor field. We illustrate this variational LCS computation on a model flow and on a velocity field obtained from a two-dimensional turbulence simulation.

II. SET-UP

We start by recalling the notation and definitions from Haller¹⁴ for the case of two-dimensional flows. We consider dynamical systems of the form

$$\dot{\mathbf{x}} = \mathbf{v}(\mathbf{x}, t), \quad \mathbf{x} \in U, \quad t \in [\alpha, \beta], \quad (1)$$

with U denoting an open, bounded subset of \mathbb{R}^2 , with the time t varying over the finite interval $[\alpha, \beta]$, and with the two-dimensional velocity, field \mathbf{v} assumed to be smooth in its arguments.

If $\mathbf{x}(t, t_0, \mathbf{x}_0)$ denotes the trajectory of Eq. (1) passing through a point \mathbf{x}_0 at time t_0 , then the flow map is defined as

$$\mathbf{F}_{t_0}^t(\mathbf{x}_0) := \mathbf{x}(t, t_0, \mathbf{x}_0).$$

This is as smooth as the vector field \mathbf{v} (see, e.g., Arnold²), enabling us to define the Cauchy–Green strain tensor field as

$$\mathbf{C}_{t_0}^{t_0+T}(\mathbf{x}_0) = (\nabla \mathbf{F}_{t_0}^{t_0+T}(\mathbf{x}_0))^* \nabla \mathbf{F}_{t_0}^{t_0+T}(\mathbf{x}_0), \quad (2)$$

with $\nabla \mathbf{F}_{t_0}^{t_0+T}$ denoting the Jacobian of $\mathbf{F}_{t_0}^{t_0+T}$, and with the star referring to matrix transposition. The tensor $\mathbf{C}_{t_0}^{t_0+T}$ is symmetric and positive definite, and hence admits two real positive eigenvalues and orthogonal real eigenvectors. The eigenvalues λ_i and corresponding unit eigenvectors ξ_i of the tensor $\mathbf{C}_{t_0}^{t_0+T}$ are defined by the relations

$$\begin{aligned} \mathbf{C}_{t_0}^{t_0+T}(\mathbf{x}_0) \xi_i(\mathbf{x}_0) &= \lambda_i(\mathbf{x}_0) \xi_i(\mathbf{x}_0), & |\xi_i(\mathbf{x}_0)| &= 1, \\ i &= 1, 2, \\ 0 < \lambda_1(\mathbf{x}_0) &\leq \lambda_2(\mathbf{x}_0). \end{aligned} \quad (3)$$

We suppress the dependence of λ_i and ξ_i on t_0 and T for notational simplicity.

If the flow is incompressible (i.e., $\nabla \cdot \mathbf{v} \equiv 0$), the eigenvalues of $\mathbf{C}_{t_0}^{t_0+T}$ also satisfy $\lambda_1(\mathbf{x}_0)\lambda_2(\mathbf{x}_0) = 1$ for any $\mathbf{x}_0 \in U$ (see Arnold²).

A. LCSs as most attracting or repelling material surfaces

The variational LCS theory in Haller¹⁴ seeks special material surfaces that act as organizing centers of observed trajectory patterns. Such material surfaces distinguish themselves by attracting or repelling nearby trajectories at locally the highest rate in the flow.

To quantify normal attraction and repulsion, consider a smooth curve $\mathcal{M}(t_0)$ at time t_0 , which is advected by the flow map into a time-evolving material line $\mathcal{M}(t) = \mathbf{F}_{t_0}^t(\mathcal{M}(t_0))$. At each point $\mathbf{x}_0 \in \mathcal{M}(t_0)$, we may select a unit normal \mathbf{n}_0 to $\mathcal{M}(t_0)$ and monitor its evolution under the linearized flow map $\nabla \mathbf{F}_{t_0}^t(\mathbf{x}_0)$. To measure how strongly repelling the material line $\mathcal{M}(t_0)$ is, we denote the length of the surface-normal component of the advected vector $\nabla \mathbf{F}_{t_0}^t(\mathbf{x}_0)\mathbf{n}_0$ by $\rho_{t_0}^t(\mathbf{x}_0, \mathbf{n}_0)$, as shown in Fig. 1. We refer to $\rho_{t_0}^t(\mathbf{x}_0, \mathbf{n}_0)$ as the *normal repulsion rate* of $\mathcal{M}(t)$ along the trajectory $\mathbf{x}(t, t_0, \mathbf{x}_0)$.

If $\rho_{t_0}^{t_0+T}(\mathbf{x}_0, \mathbf{n}_0) > 1$ holds, then $\mathcal{M}(t)$ has been overall repelling between t_0 and $t_0 + T$ along the trajectory that started from \mathbf{x}_0 . Similarly, $\rho_{t_0}^{t_0+T}(\mathbf{x}_0, \mathbf{n}_0) < 1$ implies that $\mathcal{M}(t)$ has been overall attracting along the trajectory starting from \mathbf{x}_0 .

As shown in Haller,¹⁴ the normal repulsion rate can be computed in terms of the Cauchy–Green strain tensor as

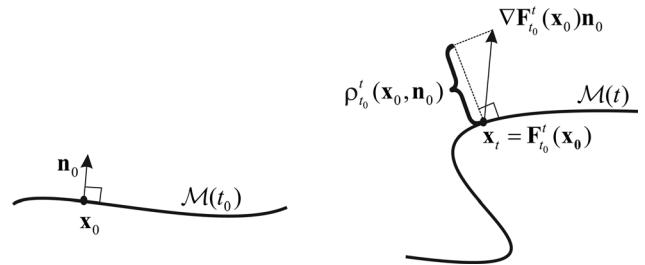


FIG. 1. The definition of the repulsion rate $\rho_{t_0}^t(\mathbf{x}_0, \mathbf{n}_0)$ at an initial point \mathbf{x}_0 of a material line $\mathcal{M}(t)$. The vector \mathbf{n}_0 denotes a unit normal to $\mathcal{M}(t_0)$ at \mathbf{x}_0 .

$$\rho_{t_0}^{t_0+T}(\mathbf{x}_0, \mathbf{n}_0) = \frac{1}{\sqrt{\left\langle \mathbf{n}_0, \left[\mathbf{C}_{t_0}^{t_0+T}(\mathbf{x}_0) \right]^{-1} \mathbf{n}_0 \right\rangle}}, \quad (4)$$

where $\langle \cdot, \cdot \rangle$ denotes the Euclidean inner product.

Using this normal repulsion rate, the main LCS definitions from Haller¹⁴ can be summarized as follows:

- A *normally repelling material line* over $[t_0, t_0 + T]$ is a compact material line segment $\mathcal{M}(t)$ on which the normal repulsion rate satisfies

$$\rho_{t_0}^{t_0+T}(\mathbf{x}_0, \mathbf{n}_0) > 1, \quad \rho_{t_0}^{t_0+T}(\mathbf{x}_0, \mathbf{n}_0) > |\nabla \mathbf{F}_{t_0}^{t_0+T}(\mathbf{x}_0) \mathbf{e}_0|$$
 for any initial point $\mathbf{x}_0 \in \mathcal{M}(t_0)$ and with unit tangent vector \mathbf{e}_0 to $\mathcal{M}(t_0)$ at \mathbf{x}_0 . The second inequality here requires any possible tangential growth within $\mathcal{M}(t)$ to be less than the growth normal to $\mathcal{M}(t)$ over the time interval $[t_0, t_0 + T]$.
- A *repelling LCS* over $[t_0, t_0 + T]$ is a normally repelling material line $\mathcal{M}(t)$ whose normal repulsion rate admits a pointwise non-degenerate maximum along $\mathcal{M}(t_0)$ among all locally C^1 -close material surfaces (cf. Fig. 2).
- An *attracting LCS* over $[t_0, t_0 + T]$ is defined as a repelling LCS over the backward time interval $[t_0 + T, t_0]$.
- Finally, a *hyperbolic LCS* over $[t_0, t_0 + T]$ is a repelling or attracting LCS over the same time interval.

By the above definitions, a material line is a hyperbolic LCS over a finite time interval I if it is locally the most repelling or attracting over I among all nearby material lines. Hence, a LCS is always associated with a time interval I over which the underlying dynamical system is known, or over which specific questions about the evolution of tracers are to be answered. There is no *a priori* reason why LCSs obtained over one time interval I should continue to exist

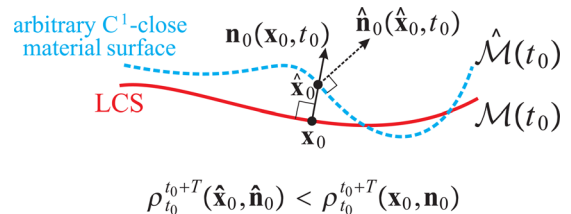


FIG. 2. (Color online) Geometry of a repelling LCS as a material line $\mathcal{M}(t_0)$ that pointwise maximizes the repulsion rate $\rho_{t_0}^{t_0+T}(\mathbf{x}_0, \mathbf{n}_0)$ relative to any nearby material line $\hat{\mathcal{M}}(t_0)$.

over different time intervals, unless those intervals are small perturbations of I . Indeed, small perturbations to I translate to small perturbations to the repulsion rate, under which a LCS—as a compact and strict local maximizer of the repulsion rate—will persist.

We now recall the main existence result on LCSs (Haller¹⁴ and Farazmand and Haller⁹), stated here specifically for two-dimensional flows. We will use the notation $\mathbf{a} \perp \gamma$ to express that a vector field \mathbf{a} is normal to a curve γ at each point of γ .

Theorem 1: [Sufficient and necessary conditions for LCSs in two-dimensional flows] Consider a compact material line $\mathcal{M}(t) \subset U$ evolving over the interval $[t_0, t_0 + T]$. Then $\mathcal{M}(t)$ is a repelling LCS over $[t_0, t_0 + T]$ if and only if all the following hold for all initial conditions $\mathbf{x}_0 \in \mathcal{M}(t_0)$:

1. $\lambda_1(\mathbf{x}_0) \neq \lambda_2(\mathbf{x}_0) > 1$;
2. $\langle \xi_2(\mathbf{x}_0), \nabla^2 \lambda_2(\mathbf{x}_0) \xi_2(\mathbf{x}_0) \rangle < 0$;
3. $\xi_2(\mathbf{x}_0) \perp \mathcal{M}(t_0)$;
4. $\langle \nabla \lambda_2(\mathbf{x}_0), \xi_2(\mathbf{x}_0) \rangle = 0$.

Condition 1 ensures that the normal repulsion rate $\rho_{t_0}^{t_0+T}(\mathbf{x}_0, \mathbf{n}_0)$ is larger than tangential stretch due to shear along the LCS. Conditions 3 and 4 together guarantee that $\rho_{t_0}^{t_0+T}$ attains a local extremum along the LCS relative to all C^1 -close material lines. Finally, condition 2 ensures that this extremum is a strict local maximum.

To relate this general result to the frequently used FTLE field $\sigma(\mathbf{x}_0) = \frac{1}{2|T|} \log \lambda_2(\mathbf{x}_0)$, note that conditions (2) and (4) are satisfied along height ridges of the $\sigma(\mathbf{x}_0)$ field.¹⁴ Therefore, by Theorem 1, such a height ridge of $\sigma(\mathbf{x}_0)$ is a repelling LCS if and only if the remaining two conditions of the theorem hold, i.e., (1) the values of σ are strictly positive along the ridge; (2) the minimal and maximal finite-time Lyapunov exponents are not equal along the ridge; and (3) the ridge is pointwise normal to the maximal strain eigenvector field $\xi_2(\mathbf{x}_0)$ (see Haller¹⁴ and Farazmand and Haller⁹ for details).

Theorem 1, however, does *neither* say that all LCSs are ridges of the FTLE field, nor say that all FTLE ridges mark LCSs. Indeed, simple examples in Haller¹⁴ show that both of these statements would be incorrect even in steady flows (cf. Haller¹⁴).

B. Reformulated LCS criterion for numerical implementation

Finding the zero set of the inner product in condition 4 of Theorem 1 tends to be numerically sensitive, which prompts us to reformulate this condition in a way that allows robust implementation. Inspecting the proof of Theorem 1 in Haller,¹⁴ we find that condition 4 serves as a necessary condition for the repulsion rate to attain a maximum on the LCS with respect to locally normal translations in the direction of ξ_2 . Indeed, the directional derivative of the repulsion rate along the vector field $\xi_2(\mathbf{x}_0)$ vanishes if

$$\frac{d}{d\epsilon} \rho'_{t_0}(\mathbf{x}_0 + \epsilon \xi_2, \xi_2)|_{\epsilon=0} = \frac{1}{2\sqrt{\lambda_2(\mathbf{x}_0)}} \langle \nabla \lambda_2(\mathbf{x}_0), \xi_2(\mathbf{x}_0) \rangle = 0, \quad (5)$$

which is equivalent to condition 4 of Theorem 1.

Motivated by this observation and by the fact that $\rho'_{t_0}(\mathbf{x}_0, \xi_2(\mathbf{x}_0)) = \sqrt{\lambda_2(\mathbf{x}_0)}$, we relax condition 4 of Theorem 1 by requiring that the average of λ_2 along $\mathcal{M}(t_0)$ be locally the largest among all nearby curves that are normal to the vector field $\xi_2(\mathbf{x}_0)$. We also relax condition 2 of the theorem from a strict inequality to one that allows equality as well. This means that we allow a LCS to have finite thickness, but insist that it has a uniquely defined local orientation. Finally, using the orthogonality of the eigenvectors $\xi_2(\mathbf{x}_0)$ and $\xi_1(\mathbf{x}_0)$, we give an equivalent form of condition 3 that will prove helpful for computational purposes.

The reformulated set of conditions obtained in this fashion is of the form

- (A) $\lambda_1(\mathbf{x}_0) \neq \lambda_2(\mathbf{x}_0) > 1$;
- (B) $\langle \xi_2(\mathbf{x}_0), \nabla^2 \lambda_2(\mathbf{x}_0) \xi_2(\mathbf{x}_0) \rangle \leq 0$;
- (C) $\xi_1(\mathbf{x}_0) \parallel \mathcal{M}(t_0)$;
- (D) $\bar{\lambda}_2(\gamma)$, the average of λ_2 over a curve γ , is maximal on $\mathcal{M}(t_0)$ among all nearby curves γ satisfying $\gamma \parallel \xi_1(\mathbf{x}_0)$.

Relaxing Theorem 1 in this fashion is consistent with numerical and laboratory observations of tracer mixing in two-dimensional, time-periodic flows. In such flows, over long enough time intervals, tracers have been observed to form striations with a clearly defined local orientation (see, e.g., Ottino²¹ and Giona *et al.*¹²). This strict local orientation in the direction of the $\xi_1(\mathbf{x}_0)$ field is still enforced by condition (C) despite the relaxed nature of conditions (B) and (D).

Observe that the relaxed conditions (A)-(D) are efficient enough to allow for the detection of LCSs even in linear flows. For instance, in the saddle-type linear velocity field $\dot{x} = x, \dot{y} = -y$, all horizontal lines qualify as attracting LCSs. Indeed, the eigenvalues and eigenvectors of the backward-time Cauchy-Green strain tensor field satisfy $\lambda_2(\mathbf{x}_0) \equiv e^T$ and $\xi_2(\mathbf{x}_0) \equiv (0, 1)$, implying that conditions (A)-(D) hold on any horizontal line $\mathcal{M}(t_0)$. When advected by the flow, any such line will be observed as an attractor for nearby tracer blobs that spread out horizontally, while becoming thinner and thinner vertically. This is to be contrasted with the well-known inability of heuristic Lagrange diagnostic tools (such as plots of FTLE or finite-size Lyapunov exponents) to explain tracer patterns in flows with constant maximal Lyapunov exponents (see Haller¹⁴ for further examples).

III. COMPUTATIONAL ASPECTS OF VARIATIONAL LCS DETECTION

According to condition (C), hyperbolic LCSs are formed by material curves that are tangent to the $\xi_1(\mathbf{x}_0)$ vector field, the eigenvector field associated with the smaller eigenvalue field $\lambda_1(\mathbf{x}_0)$ of the Cauchy-Green strain tensor field $C_{t_0}^{t_0+T}(\mathbf{x}_0)$.

Curves that are everywhere tangent to the larger eigenvector field of a two-dimensional tensor field have traditionally been called tensor lines in scientific visualization (see, e.g., Tricoche *et al.*²⁸). In order to distinguish the tensor lines tangent to ξ_1 from those tangent to ξ_2 , we refer to the lines tangent to $\xi_1(\mathbf{x}_0)$ as *strainlines* computed over the $[t_0, t_0 + T]$ time interval. The subspace $S_{\mathbf{x}_0}$ spanned by the

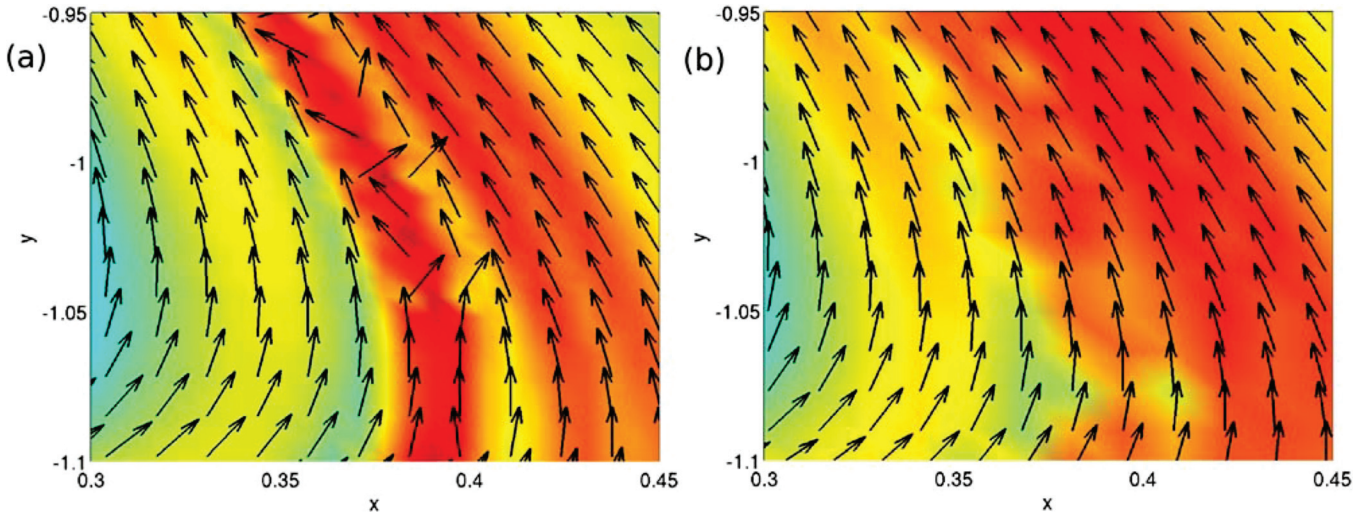


FIG. 3. (Color) (a) Computation of strain eigenvectors for the periodically forced Duffing oscillator near a repelling LCS, calculated over 670×670 grid points in the domain $[-2, 2] \times [-2, 2]$. (b) For the same computational effort, use of an auxiliary grid around a sparser initial grid returns more accurate results. The background color is the FTLE field in both plots. Note the loss of resolution for the FTLE field on the sparser grid, while the accuracy of the strain directions has increased.

eigenvector $\xi_1(\mathbf{x}_0)$ is referred to as the *strain direction* at the point \mathbf{x}_0 .

A. Numerical challenges in computing strainlines

Based on our discussion in Sec. II B, hyperbolic LCSs are captured numerically as the subset of all strainlines that satisfy the relaxed conditions (A), (B), and (D) of Theorem 1.

The following challenges arise in the numerical computation of strainlines:

- (i) *Sensitivity of the strain directions:* The eigenvectors of the Cauchy–Green strain tensor are sensitive to numerical errors. This sensitivity is even more pronounced near hyperbolic LCSs, because large deviations in nearby particles lead to large errors in the computation of the entries of the Cauchy–Green strain tensor (see Figure 3(a)). Since the conditions (A)–(D) need to be verified precisely near LCSs, the strain eigenvectors must be calculated accurately.
- (ii) *Degenerate points:* The points at which the two eigenvalues of the tensor field $\mathbf{C}_{t_0}^t(\mathbf{x}_0)$ are equal, i.e., $\lambda_1 = \lambda_2$, are referred to as degenerate points of the tensor field (see Delmarcelle and Hesselink⁷). At such points, $\mathbf{C}_{t_0}^t(\mathbf{x}_0)$ becomes a scalar multiple of the identity matrix, and hence ξ_1 and ξ_2 are ill-defined. As a result, no unique strainline exists at such a point.
- (iii) *Non-orientability of strain directions:* The eigenspaces of the Cauchy–Green strain tensor define the directions of maximal and minimal local strain. The orientation of the unit eigenvectors ξ_1 and ξ_2 within these subspaces, however, is not uniquely defined. Away from degenerate points, the unit strain eigenvectors can be chosen smoothly varying over open subsets of U . This follows from general results on the parallelizability of vector fields away from their zeros (see, e.g., Arnold²). Globally over U , however, the ξ_1

and ξ_2 vector fields may admit orientational discontinuities, i.e., along curves in the plane, the orientation of the vector field reverses (see, e.g., Fig. 4). Such orientational discontinuities are seldom removable globally; removing the discontinuity locally by reversing the sign of strain eigenvectors will only shift the discontinuity elsewhere. In differential-geometric terms, a non-removable orientational discontinuity occurs for the strain directions if the vector bundle $\{(\mathbf{x}, \mathbf{u}) : \mathbf{x} \in U, \mathbf{u} \in S_{\mathbf{x}}\}$ is non-trivial (see Abraham *et al.*¹)

In Secs. III B–III E, we address these computational challenges.

B. Accurate computation of strain directions

Since the location of LCSs, as defined in Sec. II A, is not known *a priori*, using a denser grid near LCSs is not an

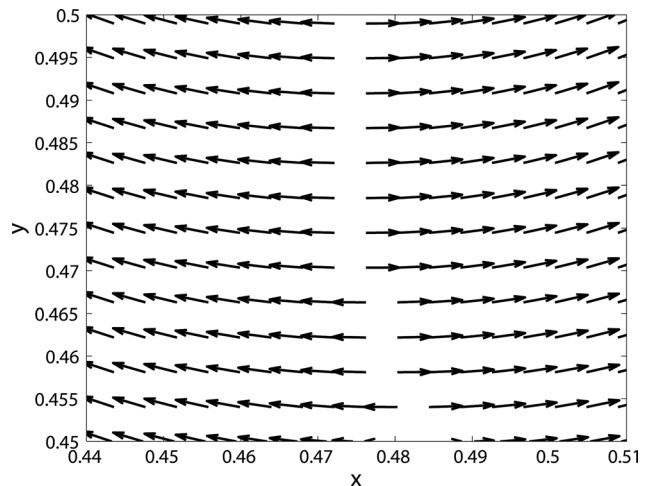


FIG. 4. An example of an orientational discontinuity of the ξ_1 field in the double-gyre example considered in Sec. V A.

option. Instead, we shall introduce a finer auxiliary grid around the original grid in order to increase the accuracy of finite differencing over the original grid.

Let $\{\mathbf{x}_j \equiv (x_j, y_j)\}_{j=1}^N$ denote the original computational grid over the domain U . To each grid point (x_j, y_j) , we assign four neighboring points defined as

$$\begin{aligned}\mathbf{x}_j^r &= (x_j + \delta x, y_j), & \mathbf{x}_j^l &= (x_j - \delta x, y_j), \\ \mathbf{x}_j^u &= (x_j, y_j + \delta y), & \mathbf{x}_j^d &= (x_j, y_j - \delta y),\end{aligned}\quad (6)$$

where δx and δy are small increments. Figure 5 shows schematically the location of the auxiliary grid points (6).

By advecting these auxiliary points in addition to the main grid, we approximate the gradient of the flow map by finite differences as

$$\nabla \mathbf{F}_{t_0}^{t_0+T}(\mathbf{x}_j) \approx \left(\frac{\mathbf{F}_{t_0}^{t_0+T}(\mathbf{x}_j^r) - \mathbf{F}_{t_0}^{t_0+T}(\mathbf{x}_j^l)}{2\delta x} \frac{\mathbf{F}_{t_0}^{t_0+T}(\mathbf{x}_j^u) - \mathbf{F}_{t_0}^{t_0+T}(\mathbf{x}_j^d)}{2\delta y} \right). \quad (7)$$

Choosing δx and δy small enough will substantially increase the numerical accuracy of $\nabla \mathbf{F}_{t_0}^{t_0+T}(\mathbf{x}_j)$, and hence of the strain eigenvector ξ_1 .

By adding four auxiliary grid points to each point in a $N \times N$ grid of initial conditions, we need to compute a total number of $5(N \times N)$ trajectories instead of $N \times N$ trajectories. Therefore, in terms of computational cost, introducing the auxiliary grid is equivalent to passing to a denser grid of $\sqrt{5}N \times \sqrt{5}N$ initial conditions. At the same time, the resulting accuracy in computing $\nabla \mathbf{F}_{t_0}^{t_0+T}(\mathbf{x}_j)$ can be controlled independently by the choice of the increments δx and δy . As a result, the accuracy of finite differencing can be increased significantly by using the auxiliary grid as opposed to just passing to a uniform $\sqrt{5}N \times \sqrt{5}N$ grid.

Figure 3 illustrates the improvement in the ξ_1 -field obtained from the use of an auxiliary grid. Figure 3(a) shows the ξ_1 -field calculated on a uniform base grid of size 670×670 , with spacing $\Delta x = \Delta y \approx 0.006$. The computation time in this case is 32.69 s. In Figure 3(b), the same ξ_1 -field is calculated by adding an auxiliary grid to a sparser base

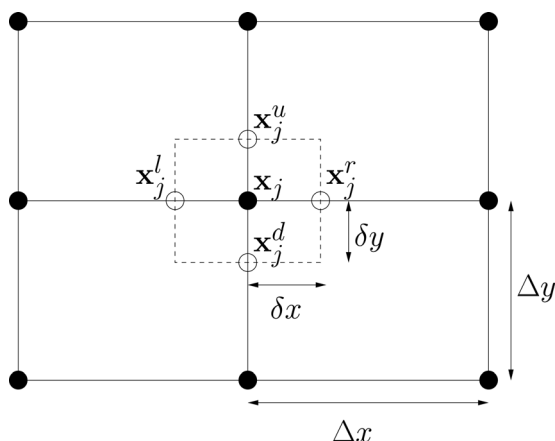


FIG. 5. Circles indicate the auxiliary grid points used for computing the strain directions with increased accuracy; black dots represent the original grid.

grid of size 300×300 , with spacing $\Delta x = \Delta y \approx 0.013$. The spacing between the auxiliary grid points is $\delta x = \delta y = 10^{-5}$. The computation time in this case is 32.44 s, i.e., slightly less than in the case of the denser base grid. The noise apparent in the case of the uniform base grid (Fig. 3(a)) is fully removed, while the computational cost remains the same.

Note that we do not require the original grid to be uniform; the same approach works on unstructured grids as well. We also add that, in our experience, the spatial distribution of $\lambda_1(\mathbf{x})$ is more noisy than that of $\lambda_2(\mathbf{x})$, even if the same numerical grid and the same explicit eigenvalue formula is used in their computation. Since these numerical errors translate to errors in the computed eigenvectors, we propose computing $\xi_2(\mathbf{x})$ first, then obtaining ξ_1 as a unit vector perpendicular to ξ_2 .

As was pointed out by Lekien and Ross,¹⁷ using the auxiliary grid for calculating the eigenvalues of the Cauchy–Green strain tensor is not suitable for measuring the amount of local repulsion (or attraction) of the material lines. This is due to the fact that the auxiliary grids ($\mathbf{x}_j^r, \mathbf{x}_j^u, \mathbf{x}_j^l, \mathbf{x}_j^d$) around a main grid point \mathbf{x}_j tend to lay on the same side of a LCS because of the small spacings δx and δy . As a result, the auxiliary grids undergo much less stretching compared to the main grid points that lay on different sides of a repelling LCS. Motivated by this observation, we compute the eigenvalues λ_1 and λ_2 using the uniform grid.

C. Computing smooth strainlines

By definition, strainlines are everywhere tangent to the unit strain eigenvector field ξ_1 . Away from repeated eigenvalues and orientational discontinuities, therefore, strainlines can be computed as smooth trajectories of the ordinary differential equation (ODE)

$$\mathbf{r}' = \xi_1(\mathbf{r}), \quad |\xi_1(\mathbf{r})| = 1. \quad (8)$$

By introducing an appropriate rescaling, we alter this ODE in a fashion so that its numerical solution yields a globally smooth set of strainlines. To achieve this, we follow the scaling suggested in Tchon *et al.*²⁷ for general tensor lines by letting

$$\begin{aligned}\mathbf{r}'(s) &= \mathbf{f}(\mathbf{r}(s), \mathbf{r}'(s - \Delta)), \\ &= \text{sign}(\xi_1(\mathbf{r}(s)), \mathbf{r}'(s - \Delta)) \alpha(\mathbf{r}(s)) \xi_1(\mathbf{r}(s)),\end{aligned}\quad (9)$$

where $\Delta > 0$ is the numerical stepsize used in integrating (9), and the scalar field $\alpha(\mathbf{x}_0)$ is defined as

$$\alpha(\mathbf{x}_0) = \left(\frac{\lambda_2(\mathbf{x}_0) - \lambda_1(\mathbf{x}_0)}{\lambda_2(\mathbf{x}_0) + \lambda_1(\mathbf{x}_0)} \right)^2. \quad (10)$$

The scaling factor $\alpha(\mathbf{x}_0)$ vanishes at degenerate points ($\lambda_1 = \lambda_2$), turning these points into fixed points (trivial strainlines). In addition, the factor $\text{sign}(\xi_1(\mathbf{r}(s)), \mathbf{r}'(s - \Delta))$ in Eq. (9) locally reverses the orientation of the vector field $\xi_1(\mathbf{r})$ along the strainline $\mathbf{r}(s)$, if needed, for smooth integration through orientational discontinuities.

D. Extraction of hyperbolic LCSs from strainlines

If $\mathcal{M}(t_0)$ lies within a strainline, then it automatically satisfies condition (C). The strainline segments along which

the further conditions (A), (B), and (D) of Sec. II B are also satisfied constitute the set of hyperbolic LCSs in the flow over the time interval $[t_0, t_0 + T]$.

The simplest approach to extracting this set of LCSs is to identify the subset $U_0 \subset U$ on which conditions (A) and (B) hold, and then integrate system (9) from initial grid points lying in U_0 to construct strainlines. This integration proceeds, in principle, until each strainline reaches the boundary of the domain U or approaches a fixed point of Eq. (9) (i.e., a degenerate point of the original ξ_1 vector field).

In most cases, however, only a segment of a strainline will be a hyperbolic LCS. Therefore, integration of a given strainline can be stopped when one of the LCS conditions (A) or (B) fails. Numerical noise may cause such failures at isolated points of the strainlines. To avoid such accidental failures, we choose to stop the strainline integration when a LCS condition fails repeatedly over a pre-set length ℓ_f of the strainline.

Having located the strainlines segments satisfying conditions (A) and (B), it remains to identify the strainlines segments that are local maximizers of the averaged maximum strain, as required by condition (D). The simplest way of doing this is to define a set L of uniformly spaced horizontal and vertical lines within the domain U_0 , and compare the values of $\bar{\lambda}_2(\gamma_0)$, the average of λ_2 on the curve γ_0 , at the neighboring intersections of all close enough strainline segments along each line in L . Intersections of the strainlines with the lines in the set L are found through linear interpolation.

If a strainline segment is found to be a local maximizer along at least one line in L , that strainline segment is labeled as a LCS (see Fig. 6). Adjacent intersections whose distance is larger than a preselect threshold, such as those encircled in Fig. 6 by a dashed ellipse, are excluded from the local maximization process.

Finally, small-scale LCSs are expected to have a negligible effect on overall pattern formation in the flow. To filter

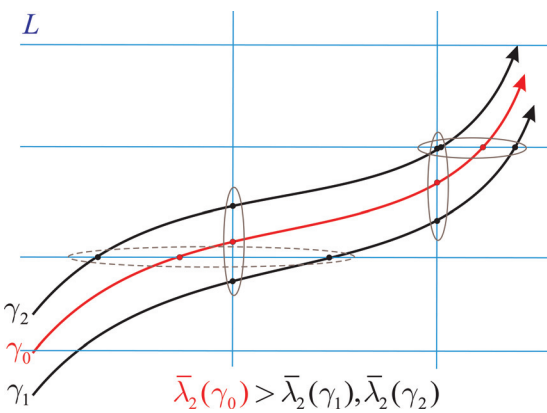


FIG. 6. (Color) Finding local maxima of the function $\bar{\lambda}_2(\gamma)$, the average of λ_2 on the curve γ , along a set L of horizontal and vertical lines. The strainline segment γ_0 is identified as a local maximizer if it is found to have a locally maximal $\bar{\lambda}_2(\gamma)$ value along at least one line in the set L . Solid ellipses indicate adjacent points at which the values of $\bar{\lambda}_2(\gamma)$ are compared. A dashed ellipse indicates points excluded from the local maximization process because of the large distances among them.

out such small structures from our computations, we discard the LCSs that are shorter than a pre-set small length ℓ_{min} .

E. Summary of variational LCS extraction algorithm in two dimensions

In Table I, we summarize the main steps of our variational LCS extraction algorithm in the form of a pseudo code. Note that if the hyperbolic LCSs are computed over a time interval $[t_0, t_0 + T]$, then repelling LCSs will be obtained at time $t = t_0$, while attracting LCSs will be identified at $t = t_0 + T$. Thus, additional advection of the attracting LCSs back to $t = t_0$ is required to obtain both attracting and repelling LCSs at the same time.

IV. ADVECTION OF HYPERBOLIC LCSs AS MATERIAL LINES

The variational theory in Haller¹⁴ constructs LCSs as material lines, i.e., fully invariant objects with zero material flux through them. The algorithm sketched in Table I locates $\mathcal{M}(t_0)$, the $t = t_0$ slice of such a LCS. To obtain the time t slice of the LCS, we need to compute the advected material curve $\mathcal{M}(t) = \mathbf{F}_{t_0}^t(\mathcal{M}(t_0))$.

Advecting a locally most repelling material line is challenging, because errors in the advection will grow exponentially and, therefore, have to be carefully managed via highly accurate numerical integration. Numerical methods have been developed for the high-precision advection of material lines via the insertion of additional material points.^{4,19} As a rule, these methods use interpolation schemes for inserting additional points into a discretely advected material line when the distance of its two adjacent points exceeds a threshold. This interpolation unavoidably introduces additional errors in the shape of the LCS in the advection process.

Our construction of a LCS as a parametrized trajectory of the strainline ODE (8) enables us to insert new points into the LCS in a dynamically consistent manner, using the underlying Lagrangian dynamics captured by the strainline field. Specifically, let γ_0 denote a LCS parametrized by $\mathbf{r} : [0, \bar{s}] \rightarrow U$, $s \mapsto \mathbf{r}(s)$. The numerical solution of Eq. (8) yields a discrete set of parameter values $\{s_i\}_{i=1}^n$ at which the set $\{\mathbf{r}(s_i)\}_{i=1}^n$ of LCS points has been determined. Increasing the number of points n on γ_0 (or equivalently decreasing the spacings $s_{i+1} - s_i$) increases the smoothness of the advected curve γ_t .

A further increase in the accuracy of the advection of the LCS is achieved by exploiting the invariance of the tangent space of the LCS under the linearized flow. The key observation is that at a point $\mathbf{r}(s_i) \in \gamma_0$ at time t_0 , the unit tangent $\xi_1(\mathbf{r}(s_i))$ to the LCS γ_0 is exactly known. Therefore, at an advected point $\mathbf{F}_{t_0}^{t_0+T}(\mathbf{r}(s_i)) \in \gamma_{t_0+T}$, a tangent vector to the advected LCS γ_{t_0+T} is given by $\nabla \mathbf{F}_{t_0}^{t_0+T}(\mathbf{r}(s_i)) \xi_1(\mathbf{r}(s_i))$, as shown in Fig. 7.

The Jacobian $\nabla \mathbf{F}_{t_0}^t(\mathbf{r}(s_i))$ can be computed locally using the auxiliary grid points introduced in Sec. III B. Note that this requires the advection of four additional neighboring points for each point $\mathbf{r}(s_i)$ on the LCS.

A geometric Hermite interpolation scheme^{6,29} of up to 6th order can be applied to the advected LCS to utilize the

TABLE I. Algorithm for computing hyperbolic LCSs from their variational theory.

```

% ode[f(x_j),x_j,Δ] refers to an ODE solver that returns the next point x_{j+1}
% along a trajectory of a vector field f(x), given the current point x_j and the stepsize Δ
%
% int[λ,R,Δ] refers to a function that computes the integral of a scalar field λ
% over a planar curve whose adjacent points are the columns of a matrix R
% the arc length increment is Δ
    •fix a grid  $\mathcal{G} \subset U$  of initial conditions;
    •fix finite time interval  $[t_0, t]$  of interest;
    •compute the Cauchy-Green strain tensor  $C'_{t_0}(x_0)$  for all  $x_0 \in \mathcal{G}$ ;
    •compute maximal strain eigenvalue  $\lambda_2(x_0)$  and corresponding unit eigenvector  $\xi_2(x_0)$  for all  $x_0 \in \mathcal{G}$ ;
    •determine sub-grid  $\mathcal{G}_0 = \mathcal{G} \cap U_0$  where  $U_0$  is the set over which conditions (A) and (B) hold;
    •select integration step  $\Delta$  along strainlines;
    •fix length  $\ell_f$  allowed for continuous failures of conditions (A) or (B) on LCSs;
    •fix  $\ell_{min} \geq 0$ , the minimum length allowed for a LCS;
    •set  $k = 0$ ; this counter will return the total number of strainlines computed.

for  $r_0 \in \mathcal{G}_0$ 
     $k = k + 1; L := 0; n := 2;$ 
     $R(1, k) := r_0$ 
     $f^{old} := \alpha(r_0)\xi_2^\perp(r_0)$ 
    while  $L < \ell_f$  and  $r_0 \in U$ 
         $f^{new} := \alpha(r_0)\xi_2^\perp(r_0)$ 
         $f^{new} := \text{sign}\langle f^{old}, f^{new} \rangle f^{new}$ 
         $r := \text{ode}[f^{new}, r_0, \Delta]$ 
        if  $r \notin U_0$ 
             $L := L + |\mathbf{R}(n - 1, k) - r|$ 
        else
             $L := 0$ 
        end if
         $R(n, k) := r$ 
         $r_0 := r; f^{old} := f^{new}; n := n + 1;$ 
    end while
     $\ell(k) = \text{int}[1, R(\cdot, k), \Delta]; \bar{\lambda}_2(k) = \text{int}[\lambda_2, R(\cdot, k), \Delta]/\ell(k)$ 
    for  $j = 1$  to  $k$ 
        if  $(\ell(j) > \ell_{min}$  and  $\bar{\lambda}_2(j) \geq \bar{\lambda}_2(j - 1)$  and  $\bar{\lambda}_2(j) \geq \bar{\lambda}_2(j + 1))$ 
            % see Sec. III D for details
            plot  $\mathbf{R}(\cdot, j)$ 
        end if
    end for
end for

```

above invariance property. The goal is to find a cubic polynomial $\mathbf{P} : [0, 1] \rightarrow U$ satisfying

$$\begin{aligned} \mathbf{P}(0) &= \tilde{\mathbf{r}}_i := \mathbf{F}_{t_0}^{t_0+T}(\mathbf{r}(s_i)), \quad \mathbf{P}(1) = \tilde{\mathbf{r}}_{i+1} := \mathbf{F}_{t_0}^{t_0+T}(\mathbf{r}(s_{i+1})), \\ \mathbf{P}'(0) \parallel \tilde{\mathbf{d}}_i &:= \nabla \mathbf{F}_{t_0}^{t_0+T}(\mathbf{r}(s_i)) \xi_1(\mathbf{r}(s_i)), \\ \mathbf{P}'(1) \parallel \tilde{\mathbf{d}}_{i+1} &:= \nabla \mathbf{F}_{t_0}^{t_0+T}(\mathbf{r}(s_{i+1})) \xi_1(\mathbf{r}(s_{i+1})). \end{aligned} \quad (11)$$

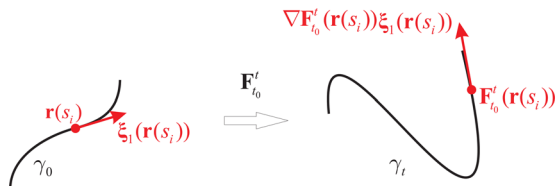


FIG. 7. (Color online) High-precision advection of a LCS, using the invariance of its tangent bundle under the linearized flow map. Note that the initial tangent vectors $\xi_1(\mathbf{r}(s_i))$ to the LCS are exactly known from the parameterized construction of the LCS at time t_0 .

This problem generally does not have a unique solution,²⁹ thus additional constraints are needed to obtain a well-defined solution. Here, we use the simplest constraint introduced in Chi *et al.*⁶ by considering the curve with minimum length among all cubic polynomials that satisfy the constraints (11). Other constraints may also be employed and may potentially lead to more accurate results in specific applications.

As shown in Chi *et al.*,⁶ a minimal length Hermite polynomial satisfies

$$\mathbf{P}(s) = (2s + 1)(s - 1)^2 \tilde{\mathbf{r}}_i + (3 - 2s)s^2 \tilde{\mathbf{r}}_{i+1} + (s - 1)^2 s \alpha_0 \tilde{\mathbf{d}}_i + (s - 1)s^2 \alpha_1 \tilde{\mathbf{d}}_{i+1}, \quad (12)$$

where

$$\alpha_0 = \frac{12\langle \tilde{\mathbf{r}}_{i+1} - \tilde{\mathbf{r}}_i, \tilde{\mathbf{d}}_i \rangle \parallel \tilde{\mathbf{d}}_{i+1} \parallel^2 + 3\langle \tilde{\mathbf{r}}_{i+1} - \tilde{\mathbf{r}}_i, \tilde{\mathbf{d}}_{i+1} \rangle \langle \tilde{\mathbf{d}}_i, \tilde{\mathbf{d}}_{i+1} \rangle}{16 \parallel \tilde{\mathbf{d}}_i \parallel^2 \parallel \tilde{\mathbf{d}}_{i+1} \parallel^2 - \langle \tilde{\mathbf{d}}_i, \tilde{\mathbf{d}}_{i+1} \rangle^2}, \quad (13a)$$

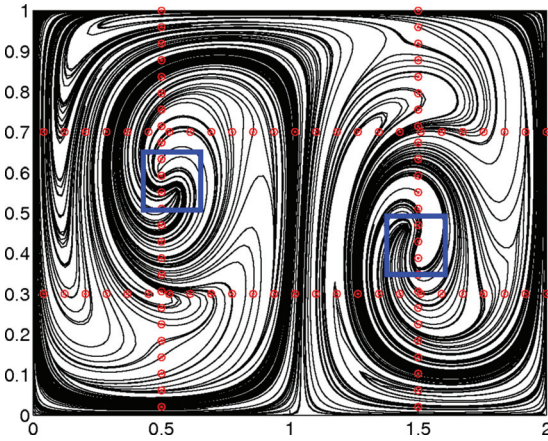


FIG. 8. (Color) Strainlines computed for system (14) using the algorithm summarized in Table I. Blue squares show the approximate location of degenerate points for the ξ_1 strain vector field.

$$\alpha_1 = \frac{12\langle \tilde{\mathbf{r}}_{i+1} - \tilde{\mathbf{r}}_i, \tilde{\mathbf{d}}_{i+1} \rangle \|\tilde{\mathbf{d}}_i\|^2 + 3\langle \tilde{\mathbf{r}}_{i+1} - \tilde{\mathbf{r}}_i, \tilde{\mathbf{d}}_i \rangle \langle \tilde{\mathbf{d}}_i, \tilde{\mathbf{d}}_{i+1} \rangle}{16 \|\tilde{\mathbf{d}}_i\|^2 \|\tilde{\mathbf{d}}_{i+1}\|^2 - \langle \tilde{\mathbf{d}}_i, \tilde{\mathbf{d}}_{i+1} \rangle^2}. \quad (13b)$$

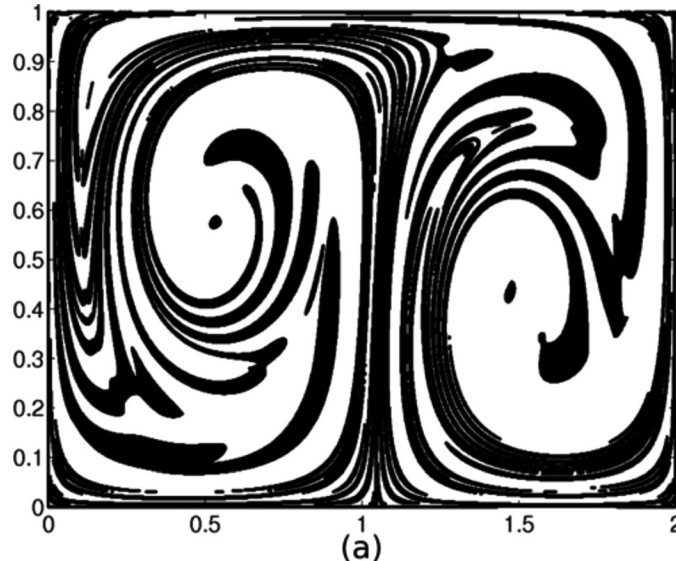
The performance of this high-accuracy LCS-advection method is illustrated in Sec. V B.

V. EXAMPLES

We now demonstrate the performance of the variational LCS computation summarized in Table I on two unsteady velocity fields. The first is an unsteady double-gyre model that has been used extensively as a test case for locating LCSs from various indicators (see Shadden *et al.*²⁶). The second velocity field is obtained from a direct numerical simulation of two-dimensional turbulence.

A. The double gyre

The double gyre model consists of a pair of counter-rotating gyres, with a time-periodic perturbation. In terms of the planar variable $\mathbf{x} = (x, y)$, this system can be written as



(a)

$$\dot{\mathbf{x}} = \pi A \begin{pmatrix} -\sin(\pi f(x)) \cos(\pi y) \\ \cos(\pi f(x)) \sin(\pi y) \frac{\partial f}{\partial x} \end{pmatrix}, \quad (14)$$

where

$$f(x, t) = a(t)x^2 + b(t)x,$$

$$a(t) = \epsilon \sin(\omega t),$$

$$b(t) = 1 - 2\epsilon \sin(\omega t).$$

For our computations, we use the same parameter values as in Shadden *et al.*,²⁶ i.e., $\epsilon = 0.1$, $A = 0.1$, and $\omega = 2\pi/10$. The starting time is $t_0 = 0$, and the integration time is $T = 20$ (i.e., two forcing periods). The Cauchy–Green strain tensor is calculated on the domain $U = [0, 2] \times [0, 1]$ over a uniform grid \mathcal{G} of 1000×500 points. As a result, the mesh size for the uniform grid is approximately $\Delta x = \Delta y = 0.002$. For computing the eigenvectors of $\mathbf{C}_{t_0}^{t_0+T}$, an auxiliary grid of size $\delta x = \delta y = 10^{-5}$ is used.

Figure 8 shows a set of strainlines calculated for system (14), with red circles indicating initial positions of the strainlines. Out of all strainlines shown in the figure, only the streamline segments satisfying conditions (A), (B), and (D) will qualify as repelling LCSs.

We now identify the streamline segments satisfying the LCS conditions (A) and (B) by computing the set \mathcal{G}_0 defined in Table I. Shown in Fig. 9(a), the set \mathcal{G}_0 consists of 136 607 grid points.

To eliminate redundant computations within this set, we follow an approach similar to the one adopted by Lipinski and Mohseni¹⁸ in a different context. Specifically, we reduce the set of strain initial conditions considered further from \mathcal{G}_0 to its intersections with a set of four horizontal and four vertical lines, as shown in Fig. 9(b). This remaining set of strain initial conditions consists of 1422 grid points, almost two orders of magnitude less than the number of points in \mathcal{G}_0 .

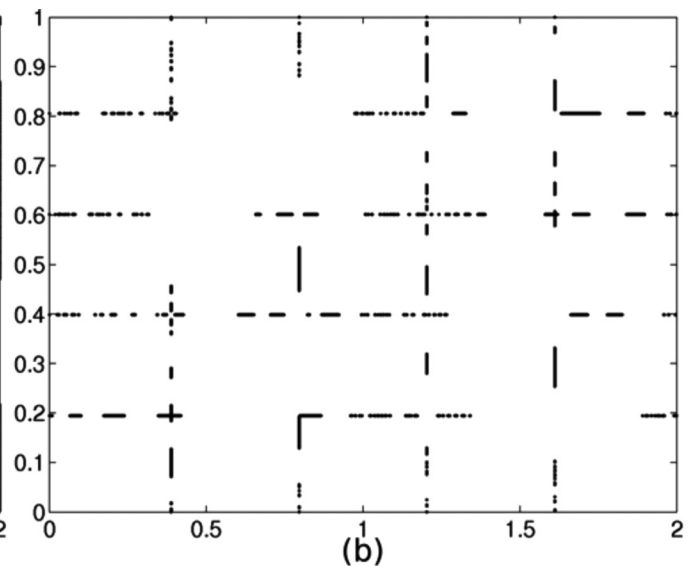


FIG. 9. (a) The set \mathcal{G}_0 for the double gyre of system (14). (b) The intersection of the set \mathcal{G}_0 with four vertical and four horizontal lines.

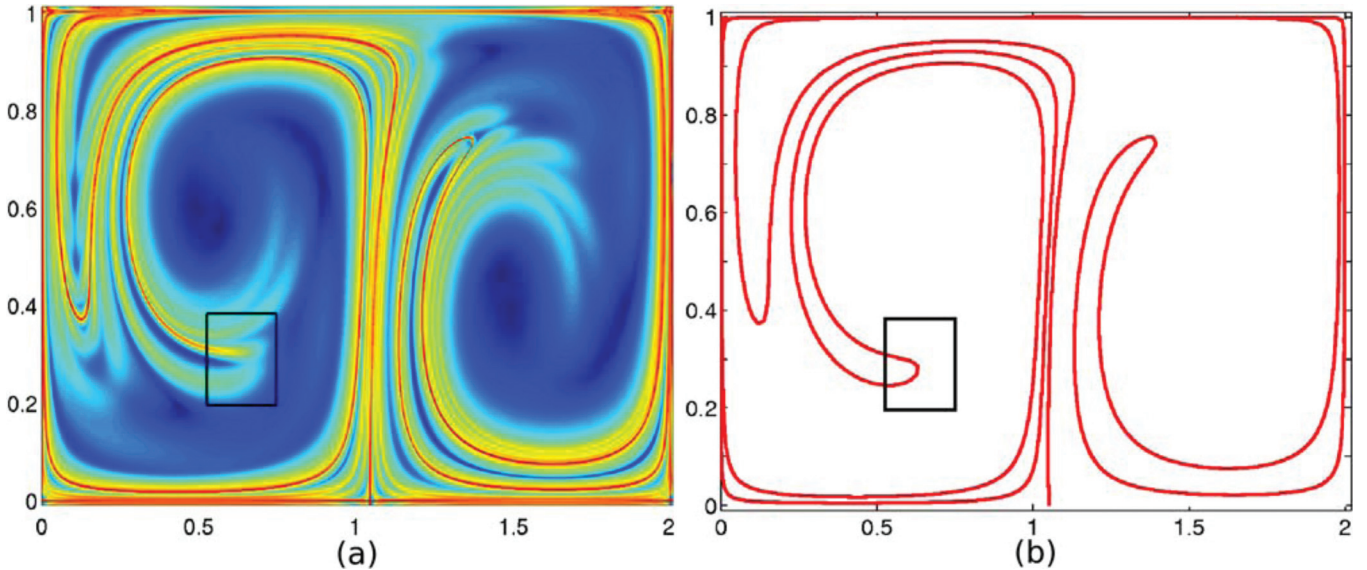


FIG. 10. (Color) (a) The forward time FTLE field for the double-gyre model; integration time is $T=20$. (b) The red curve is a strainline segment that qualifies as a repelling LCS by satisfying conditions (A), (B), and (D). The filtering parameters are chosen as $\ell_f = 0.2$, $\ell_{min} = 1$.

Among the strainlines initiated from the initial conditions shown in Fig. 9(b), only the ones along which condition (D) is satisfied qualify as repelling LCSs. For instance, for the filtering parameter values $\ell_f = 0.2$ and $\ell_{min} = 1$, only the single strainline segment shown in Fig. 10(b) qualifies as a repelling LCS over the time interval $[0, 20]$.

Note that the strainline integration stops once it reaches the boundary. In order to obtain longer strainlines (and longer LCSs as a result), a slightly larger domain $U = [-0.02, 2.02] \times [-0.01, 1.01]$ is used in Figure 10.

This well-studied example demonstrates the advantages of the variational LCS computation over simply using the FTLE field to infer the location of LCSs:

1. The FTLE field in Figure 10(a) gives an intuitive idea about the location of a LCS. By contrast, Figure 10(b) is based on a mathematical existence result (Theorem 1) that guarantees the existence of a repelling LCS. Note that none of the strainlines (and hence none of the LCSs) coincide precisely with the FTLE ridge. Instead, a part of a FTLE ridge that remains close to strainlines satisfying conditions (A), (B), and (D) is a good approximation for a LCS.
2. The ridge of the FTLE field in Figure 10(a) is easy to recognize visually. Extracting such ridges for further analysis, however, leads to an image-processing problem that ultimately yields a set of points approximating the LCS candidate (see Lipinski and Mohseni¹⁸ and Senatore and Ross²⁵). By contrast, the strainline segment in Figure 10(a) is given in the form of a smoothly parametrized curve—a trajectory of the ODE (8)—with precisely defined repulsion properties. This curve can be obtained at arbitrarily high resolution by selecting a small enough step-size Δ in solving the scaled strainline ODE (9).
3. Even if a FTLE ridge is not well-pronounced, as long as it correctly signals a nearby LCS, the strainlines will capture that LCS sharply. Indeed, the FTLE ridge shown in Figure 10(a) fades away in the black rectangle, yet the

corresponding LCS is captured without interruption by the strainline shown in Figure 10(b).

Similar results and conclusions hold for attracting LCSs, with the computations performed in backward time.

B. Randomly forced turbulent flow

In our second example, we test our numerical algorithm for variational LCS detection on a direct numerical simulation of two-dimensional turbulence. The velocity field \mathbf{v} is obtained as the numerical solution of the modified Navier–Stokes equation,

$$\partial_t \mathbf{v} + \mathbf{v} \cdot \nabla \mathbf{v} = -\nabla p - \nu_u \Delta^2 \mathbf{v} + \nu_i \Delta^{-1} \mathbf{v} + \mathbf{f}, \quad \nabla \cdot \mathbf{v} = 0, \quad (15)$$

by a pseudo-spectral method with 1024^2 Fourier modes. We use a Krylov-subspace method⁸ for temporal integration. We set the hyperviscosity as $\nu_u = 2 \times 10^{-9}$ to shift the dissipation to smaller scales while keeping the resolution relatively low. Energy is removed from large scales by the hypoviscosity $\nu_i = 1$ to prevent energy accumulation at the largest available scales. The forcing \mathbf{f} is mono-scale (active at the wavenumber $k = 2$) with random phase. The amplitude of the forcing changes in time, ensuring statistically stationary state. Equation (15) is solved on the spatial domain $[0, 2\pi] \times [0, 2\pi]$ with periodic boundary conditions, over the time interval $[0, 100]$ (see Refs. 5 and 10 for similar simulations of the same equation).

The hyperbolic LCS extraction algorithm again follows Table I. To implement condition (D), we fix L as a set of 20 equally spaced vertical and 20 horizontal lines. Local minima of $\bar{\lambda}_2(\gamma)$ are only kept if the neighboring strainline segments with weaker $\bar{\lambda}_2$ values are no more than 0.05 apart along the horizontal or vertical lines.

Figure 11 shows attracting LCSs extracted at time $t_0 = 70$ from a backward-time calculation with integration time $T = -30$ over a grid of 512×512 points.

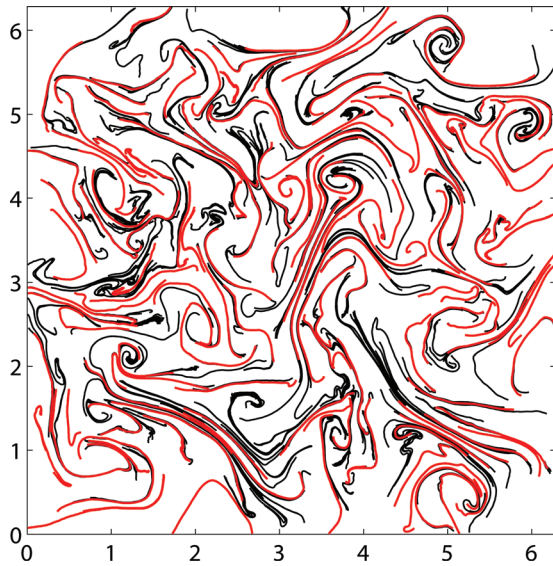


FIG. 11. (Color) Attracting LCSs at $t_0 = 70$ with integration time $T = -30$ in the flow generated by the turbulent velocity field solving Eq. (15). The black strainline segments satisfying the LCS conditions (A) and (B) are extracted by the algorithm described in Table I. The filtering parameter values in this computation are set to $\ell_f = 0.1$ and $\ell_{min} = 0.3 \max(\ell) = 1.19$. The red strainline segments also satisfy condition (D), and hence are attracting LCSs that serve as cores of tracer patterns.

Figure 12 shows the red attracting LCSs of Figure 11 in black, but now with the FTLE field superimposed for comparison. A closeup demonstrates how strainlines yield sharp LCSs, while the FTLE field remains blurry. More importantly, while the FTLE produces an attractive picture, its ridges tend to turn into spiraling shear maxima near vortex cores, as revealed by the inset in Figure 12. These ridges, therefore, constitute false predictions of hyperbolic LCSs. By contrast, the strainline segments are shown in the inset

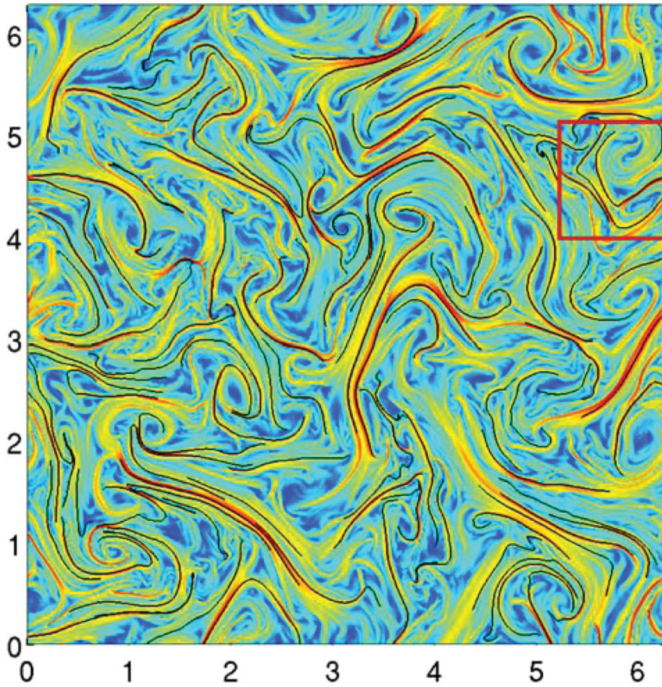


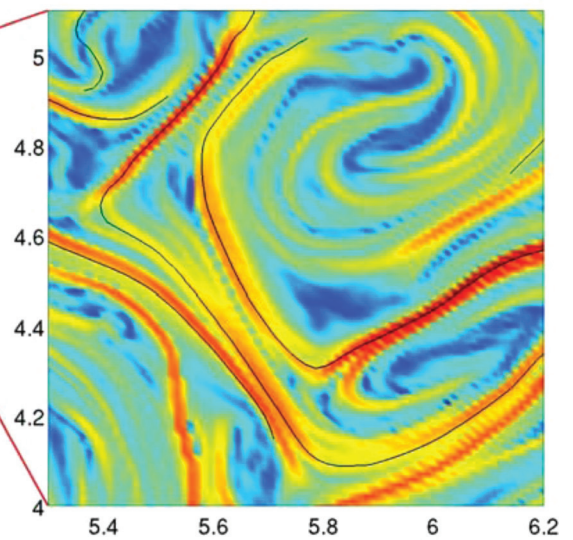
FIG. 12. (Color) Attracting LCSs for the turbulent velocity field, with the FTLE field as shown in the background.

satisfying conditions (A), (B), and (D), and hence are guaranteed to act as material lines shaping the skeleton of tracer patterns.

Finally, we demonstrate the performance of the advection scheme introduced in Sec. IV on this example. Figure 13(a) shows the initial location (dashed curve) of an attracting LCS at time $t_0 = 70$. The length of an attracting LCS shrinks exponentially in backward-time advection. As a result, comparing the performance of different interpolation schemes for inserting new points into the LCS would be challenging. For this reason, we choose to advect the LCS forward to $t = 90$. No claims about the hyperbolicity of this material line can be made over the interval [40, 90], given that its hyperbolicity was only established over the interval [40, 70]. A total number of 222 equidistant points on the LCS is advected forward to time $t = 90$ (solid curve in Figure 13(a)). Note that the number of points on the advected LCS can be arbitrarily increased by reducing the integration step size of the strainline equation (8).

In order to examine the Hermite interpolation scheme of Sec. IV, we advect a subset of the above mentioned LCS with 23 equidistant points from time $t_0 = 70$ to $t = 90$. The Hermite interpolation (12) is then applied to each of the two consecutive points. Figure 13(b) shows the advected image of these 23 points together with the Hermite interpolant (red curve). The “ground truth” advected LCS with 222 points (black curve) is given for comparison. The blue line is the linearly interpolated curve. This example shows that the Hermite interpolation scheme introduced in Sec. IV produces a smooth curve that closely mimics the actual evolving LCS, although the interpolation is based on a sparse subset of the full LCS.

Finally, note that the error in the advected position of the LCS leads to non-zero material flux through the LCS. If



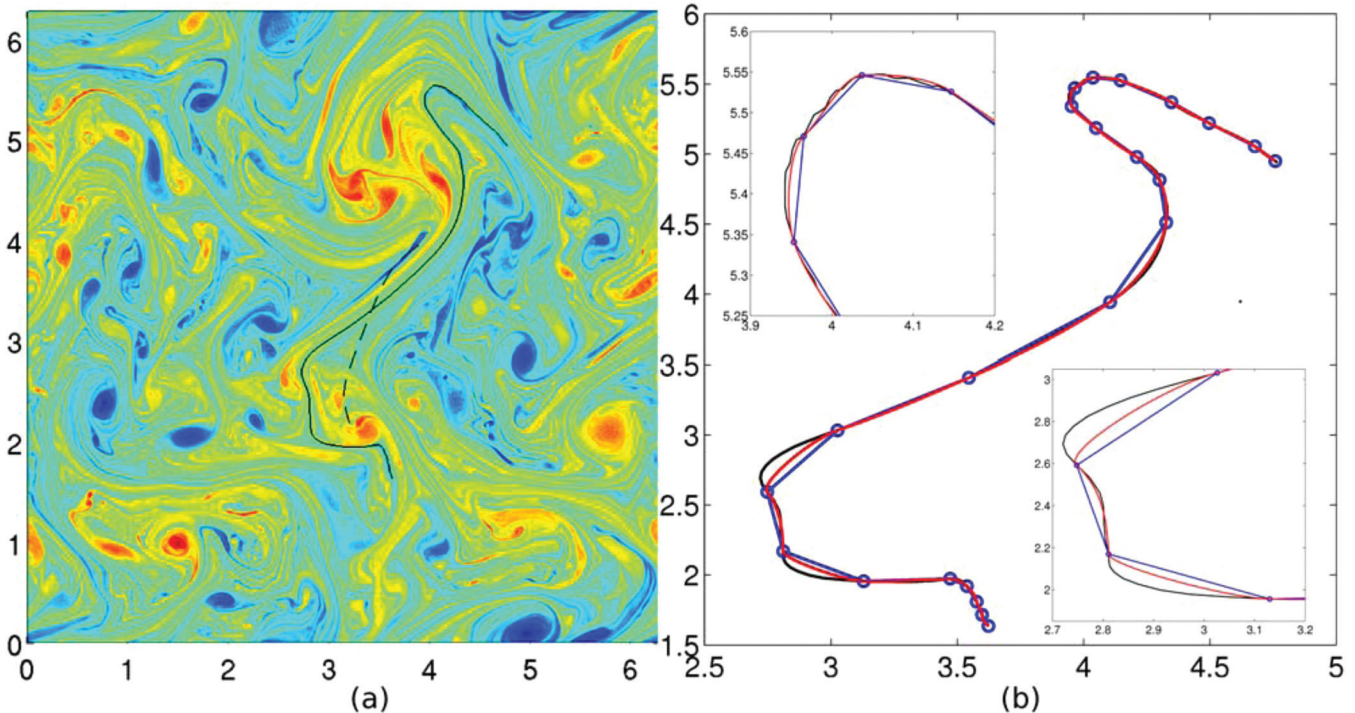


FIG. 13. (Color) (a) An attracting LCS at time $t_0 = 70$ (dashed) and its advected image at time $t_0 + T = 90$ (solid). The vorticity field at time $t_0 + T = 90$ is given in the background. (b) Black: the advected image of the LCS with 222 points, red: the advected image with 23 points and Hermite interpolation, and blue: the advected image with 23 points and linear interpolation. The insets show closeups of the same curves.

the exact zero-flux property of the LCS is of importance, a sufficient number of points on the LCS must be advected with an accurate interpolation scheme to minimize this inevitable, numerically generated flux.

VI. CONCLUSIONS

We have discussed a numerical implementation of the recent variational theory of hyperbolic LCSs for two-dimensional flows (Haller¹⁴ and Farazmand and Haller⁹). Based on exact mathematical theorems, the algorithm developed here renders attracting and repelling LCSs in the form of smoothly parametrized strainlines.

The strainlines $\mathcal{M}(t_0)$ are a subset of the tensor lines associated with the Cauchy-Green strain tensor field $\mathbf{C}_{t_0}^{t_0+T}(\mathbf{x}_0)$, and hence are trajectories of an ordinary differential equation. As ODE trajectories, the strainlines can be obtained with arbitrarily high precision at relatively low numerical cost. Well-resolved strainlines can further be advected by the flow map to yield LCSs as material lines $\mathcal{M}(t) = \mathbf{F}'_{t_0}(\mathcal{M}(t_0))$. We have shown how the known tangents of $\mathcal{M}(t)$ can be used as input to a higher-order Hermite interpolation scheme that further increases the precision of LCS advection. The evolving LCS, $\mathcal{M}(t)$, obtained in this fashion is fully Lagrangian (i.e., the material flux through it is zero) and acts as a core of observed mixing patterns by its locally most attracting or repelling nature.

Our approach is different from available Lagrangian diagnostic tools (FTLE, finite-size Lyapunov exponents, relative or absolute dispersion, etc), whose outputs are plots of scalar distributions (as opposed to parametrized curves) that are yet to be connected to LCSs mathematically. Such tools

detect shear and strain together, and hence may produce false positives for hyperbolic behavior (cf. Haller¹⁴ and the example in Sec. V B).

Clearly, additional effort is required in the numerical implementation of variational LCS theory compared to plotting diagnostic fields, even though the final computation times are roughly equal, given the absolute dominance of trajectory-advection in all Lagrangian calculations. In a number of applications, illustration of coherent features through diagnostic quantities is sufficient, and the details and exact nature of coherent structures, including false positives and negatives, are unimportant. By contrast, the present numerical algorithm is geared towards using LCSs in critical situations, where accurate now-casting and short-term forecasting without false positives or negatives is a must. An example is the short-term prediction of instabilities in environmental contamination patterns, such as an oil spill. In that context, the algorithm described here has delivered highly accurate short-term forecasts without any reliance on future velocities obtained from Eulerian forecasting models (Olascoaga and Haller²⁰).

The theorems in Haller¹⁴ and Farazmand and Haller⁹ are stated for general n -dimensional flows, and hence the extension of the present algorithm to higher-dimensional flows is, in principle, possible. In three-dimensional flows, for instance, the role of strainlines is taken over by two-dimensional strainsurfaces that are everywhere normal to the eigenvector field $\xi_3(\mathbf{x})$ of the largest Cauchy-Green eigenvalue field $\lambda_3(\mathbf{x})$. Strainsurfaces, however, no longer satisfy ODEs: they have to be located as solutions of a partial differential equation (PDE). A unique solution to these PDEs is often impossible to find as pointed out by Palmerius *et al.*,²² but numerical

algorithms providing self-consistent solutions have been developed (see, e.g., Frankot and Chellappa¹¹).

Beyond a generalization to higher dimensions, the extension of the present algorithm to extract non-hyperbolic LCSs (such as shear jets and eddies) is of great practical interest. Developments in the underlying theory and computational approach will appear in Haller *et al.*¹⁵

ACKNOWLEDGMENTS

We are grateful to Ronny Peikert and Xavier Tricochet for their helpful comments and for pointing out Refs. 28 and 7. We are also thankful to Francisco Beron–Vera for his suggestions and for coining the word *strainline*. This research was supported by NSERC Grant 401839-11.

- ¹Abraham, R., Marsden, J. E., and Ratiu, T., *Manifolds, Tensor Analysis and Applications* (Springer, Berlin, 1988).
- ²Arnold, V. I., *Mathematical Methods of Classical Mechanics* (Springer, Berlin, 1978).
- ³Boffetta, G., Lacorata, G., Redaelli, G., and Vulpiani, A., “Detecting barriers to transport: A review of different techniques,” *Physica D* **159**, 58 (2001).
- ⁴Broer, H. W., Osinga, H. M., and Vegter, G., “Algorithms for computing normally hyperbolic invariant manifolds,” *Z. Angew. Math. Phys.* **48**, 480 (1997).
- ⁵Chen, S., Ecke, R. E., Eyink, G. L., Wang, X., and Xiao, Z., “Physical mechanism of the two-dimensional enstrophy cascade,” *Phys. Rev. Lett.* **91**, 214501 (2003).
- ⁶Chi, J., Zhang, Y., and Zhang, C., in *IEEE 8th International Conference on Computer and Information Technology Workshops* (IEEE Computer Society, Washington, DC, 2008), pp. 330–335.
- ⁷Delmarcelle, T. and Hessellink, L., “The topology of symmetric, second-order tensor fields,” Proc. IEEE Visualization, 140 (1994).
- ⁸Edwards, W. S., Tuckerman, L. S., Friesner, R. A., and Sorensen, D. C., “Krylov methods for the incompressible Navier–Stokes equations,” *J. Comput. Phys.* **110**, 82 (1994).
- ⁹Farazmand, M. and Haller, G., “Erratum and addendum to ‘A variational theory of hyperbolic Lagrangian coherent structures,’ *Physica D* **240**, 574–598 (2011),” *Physica D* **241**, 439 (2012).
- ¹⁰Farazmand, M., Kevlahan, N. K.-R., and Protas, B., “Controlling the dual cascade of two-dimensional turbulence,” *J. Fluid Mech.* **668**, 202 (2011).
- ¹¹Frankot, R. T. and Chellappa, R., “A method for enforcing integrability in shape from shading algorithms,” *IEEE Trans. Pattern Anal. Mach. Intell.* **10**, 439 (1988).
- ¹²Giona, M., Adrover, A., Muzzio, F. J., Cerbelli, S., and Alvarez, M. M., “The geometry of mixing in time-periodic chaotic flows. I. Asymptotic directionality in physically realizable flows and global invariant properties,” *Physica D* **132**, 298 (1999).
- ¹³Haller, G., “Distinguished material surfaces and coherent structures in 3D fluid flows,” *Physica D* **149**, 248 (2001).
- ¹⁴Haller, G., “A variational theory of hyperbolic Lagrangian coherent structures,” *Physica D* **240**, 574 (2011).
- ¹⁵Haller, G., Farazmand, M., and Beron-Vera, F. J., “A variational theory of shear-type Lagrangian coherent structures” (preprint).
- ¹⁶Haller, G. and Yuan, G.-C., “Lagrangian coherent structures and mixing in two-dimensional turbulence,” *Physica D* **147**, 352 (2000).
- ¹⁷Lekien, F. and Ross, S. D., “The computation of finite-time Lyapunov exponents on unstructured meshes and for non-Euclidean manifolds,” *Chaos* **20**, 017505 (2010).
- ¹⁸Lipinski, D. and Mohseni, K., “A ridge tracking algorithm and error estimate for efficient computation of Lagrangian coherent structures,” *Chaos* **20**, 017504 (2010).
- ¹⁹Mancho, A. M., Small, D., Wiggins, S., and Ide, K., “Computation of stable and unstable manifolds of hyperbolic trajectories in two-dimensional, aperiodically time-dependent vector fields,” *Physica D* **182**, 188 (2003).
- ²⁰Olascoaga, M. J. and Haller, G., “Forecasting sudden changes in environmental contamination patterns,” Proc. Natl. Acad. Sci. (in press).
- ²¹Ottino, J. M., *The Kinematics of Mixing: Stretching, Transport and Chaos* (Cambridge University Press, Cambridge, 1997).
- ²²Palmerius, K. L., Cooper, M., and Ynnerman, A., “Flow field visualization using vector field perpendicular surface,” in *Proceeding SCCG ’09 (Proceedings of the 2009 Spring Conference on Computer Graphics, Budmerice, Slovakia)*, 2009.
- ²³Peacock, T. and Dabiri, J., “Focus issue: Lagrangian coherent structures,” *Chaos* **20**, 017501 2010.
- ²⁴Provenzale, A., “Transport by coherent barotropic vortices,” *Annu. Rev. Fluid Mech.* **31**, 55 (1999).
- ²⁵Senatore, C. and Ross, S. D., “Detection and characterization of transport barriers in complex flows via ridge extraction of the finite-time Lyapunov exponent field,” *Int. J. Numer. Methods Eng.* **86**, 1163 (2011).
- ²⁶Shadden, S. C., Lekien, F., and Marsden, J. E., “Definition and properties of Lagrangian coherent structures from finite-time Lyapunov exponents in two-dimensional aperiodic flows,” *Physica D* **212**, 271 (2005).
- ²⁷Tchon, K., Domptierre, J., Vallet, M. G., Guibault, F., and Camarero, R., “Two-dimensional metric tensor visualization using pseudo-meshes,” *Eng. Comput.* **22**, 121 (2006).
- ²⁸Tricoche, X., Scheuermann, G., and Hagen, H., “A topology simplification method for 2D vector fields,” Proc. IEEE Visualization, 359 (2000).
- ²⁹Yong, J.-H. and Cheng, F., “Geometric Hermite curves with minimum strain energy,” *Comput. Aided Geom. Des.* **21**, 281 (2004).